Chalcogenide Letters Vol. 22, No. 4, April 2025, p. 277 - 292

Improved electrochemical performance of nanostructured CO_3O_4/CO_3S_4 composite for supercapacitor applications

J. Ahmad [a], Naeem-Ur-Rehman [a,*], M. Shakil [a], M. Saleem [a], K. Mahmood [b], A. Ali [b], M. Imran [c], S. Sharif [d], Hosam O. Elansary [e], S. Mumtaz [f], A. D. Khalid [g]
[a] *Institute of Physics, The Islamia University of Bahawalpur, Bahawalpur, Pakistan*
[b] *Department of Physics, Government College University, Faisalabad, Pakistan*
[c] *Beijing Key Laboratory of Environmental Science and Engineering, School of Materials Science and Engineering, Beijing Institute of Technology, P.R. China*
[d] *Department of Chemistry, Materials Chemistry Laboratory, Govt. College University, Lahore, Pakistan*
[e] *Department of Plant Production, College of Food & Agricultural Sciences, King Saud University, P.O. Box 2460, Riyadh 11451, Saudi Arabia.*
[f] *Department of Chemical and Biological Engineering, Gachon University, 1342 Seongnamdaero, Sujeong-gu, Seongnam-si 13120, Republic of Korea*
[g] *University Institute of Radiological Sciences and Medical Imaging Technology, The University of Lahore, Lahore, Pakistan*

This study highlights the superior electrochemical performance of Co_3O_4/Co_3S_4 composite nanoparticles for supercapacitors, compared to individual Co_3O_4 and Co_3S_4, synthesized using sol-gel, co-precipitation, and mechanical alloying methods. The composite combines pseudocapacitance and electric double-layer capacitance, as evidenced by cyclic voltammetry. It exhibits a specific capacitance of 722.9 F/g at 0.5 A/g and an energy density of 73.8 Wh/kg at 405 W/kg. Electrochemical impedance spectroscopy reveals low charge transfer resistance and excellent cycling stability is achieved, with 98.5% capacitance retention after 1500 cycles. These results confirm the composite's potential for high-performance energy storage applications.

(Received December 4, 2024; Accepted April 1, 2025)

Keywords: Nanostructure, Semiconducting, Oxide and sulphide, Composite, Energy storage

1. Introduction

The overconsumption of fossil fuels has become a significant global issue. One effective approach to overcome this global issue is to develop renewable energy sources that are cost-effective, ecologically friendly, highly efficient, and offer sustainable electrical stability [1]. In the same way, the energy storage capability of devices is also an option that can help to overcome the energy problem and provide energy in the absence of any energy source. Lithium-ion batteries, introduced in 1991, have become the best common energy source and are extensively used in convenient electronic devices. However, their comprehensive application in the automotive industry is limited due to safety concerns and low energy density (Ed) [2]. As an alternative, sodium-ion batteries have been anticipated and actively researched due to their inferior reactivity and the greater abundance of sodium equated to lithium [3].

Additionally, supercapacitors (SCs) are considered capable energy storage devices (ESDs) due to their extraordinary theoretical Ed and rapid charge/discharge capabilities, making them superior to batteries [4]. Supercapacitors as critical electrical ESDs have been broadly studied because of their excellent cyclic stability, best specific power density (Pd), and fast charging-

---

[*] Corresponding authors: naeem.rehman@iub.edu.pk

https://doi.org/10.15251/CL.2025.224.277

discharging rates [5]. The performance of these devices is primarily estimated by electrode materials (EMs) [6]. The best electrode material considered the major challenge for promoting and commercializing these capacitors, can be the game changer for this technology [7].

To date, commonly used EMs include, conducting polymer materials (CPMs) [8], transition metal oxides (TMOs) [9], transition metal sulfides (TMSs) [10], carbon materials (CMs) [11], and other compounds. However, each of these materials has its shortcomings. For instance, CMs tend to restack, which reduces their specific surface area—a crucial indicator of performance [12]. CPMs also face structural collapse during long-term charge/discharge cycles [13]. However, these shortcomings of CMs and CPMs render them less suitable as electrode materials.

Due to the aforementioned reasons, TMOs got huge attention from researchers due to their variable oxidation states and high charge storage capacity [14]. TMOs are considered suitable electrode materials due to their best reversible faradic reactions, attributed to their valence flexibility. They exhibit several outstanding characteristics, including (i) low cost, (ii) serving as support materials for numerous noble metal nanostructures [15], (iii) minimizing industrial operation costs due to their high abundance on Earth [16], (iv) offering appealing catalytic properties [17] and (v) demonstrating higher energy storage abilities [18]. Due to these causes, earth-abundant transition metals-based nanostructured materials are considered potential candidates for electrochemical applications. Recent studies have revealed that TMOs with various dimensions and unique morphologies possess exceptional specific capacitance and electrochemical efficiency [19]. However, TMOs comparatively have lower electron conductivity than carbon materials and CPMs, which may reduce their specific capacity [20]. To address this issue, significant progress has been made in studying metal sulfides widely used in supercapacitors [21] and batteries [22].

Transition metal sulfides (TMSs) exhibit adaptable element configurations, extraordinary crystal assemblies, varied valence positions, and numerous structures [23]. Additionally, TMSs are low-cost and offer better electrical conductivity than their oxide counterparts due to their smaller sulfur electronegativity compared to oxygen, making them promising for electrochemical applications [24]. Cobalt-based sulfides, such as CoS, CoS_2, Co_3S_4, and Co_9S_8, exhibit different stoichiometries, crystal structures, and unique electronic, optical, physical, and chemical properties [25]. Among them, Co_3S_4 exhibits excellent stability attributed to its best thermal stability and high electronic conductivity [26]. These properties enable extensive applications in electrochemical supercapacitors.

Cobalt-based sulfides have significant potential for supercapacitor applications, but their use is limited by instability, sluggish reaction kinetics, and a tendency to aggregate. Solving these issues would lead to an increase in energy storage capacity and stability [27]. The most common approach involves altering the morphology of sulfides based on the Cobalt and combining them with additional purposeful constituents, namely conductive polymers, precious metal nanostructures, and carbon materials [28]. Recently, transition metal elements like Ni, Fe, Mn, Cu, and Zn have been reported to enhance the catalytic aptitude of sulfides based on cobalt [29].

Among transition metal sulfides and oxides, Co_3O_4 and Co_3S_4 are considered the best options as EMs for capacitors because of their cost-effectiveness, great theoretical specific capacity, and relatively small environmental impact [30]. Nevertheless, the deprived cycle stability of Co_3S_4 and the lesser energy density of Co_3O_4 remain key limitations to their further advancement [31]. To tackle these issues, considerable research has focused on developing composite electrode materials as a straightforward and efficient approach [32]. The heterojunctions at the interface play the best role in facilitating charge transport and enhancing surface reaction kinetics by providing an internal electric field [33]. In their study, J. Yan et al. synthesized Co_3O_4, which demonstrated a specific capacitance (Cs) of 261 F/g at a current density of 0.25 A/g [34]. M. Zhu et al. synthesized Co_3S_4 nanopolyhedra, observing a Cs of 353 F/g at 10 A/g, with a capacitance retention (Cr) of 86.4% after 5,000 no of cycles at 4 A/g. Additionally, an Ed of 20.7 Wh/kg and a Pd of 716 W/kg were achieved [35]. W. Zhang et al. synthesized N-$CoMoO_4$@Co_3O_4 double-shell nanoboxes, achieving a maximum Cs of 520 F/g [36]. Y. Gu et al. synthesized a PANI/Fe_2O_3/CNF composite electrode material, exhibiting an impressive Cs of 603 F/g at 1 A/g, with an E of 18.29 Wh/kg and a P of 500 W/kg [37]. G. Liu et al. prepared a CNF@CoNi(1:4)S composite, achieving a Cs of 617.78 F/g at 0.5 A/g, with a maximum E of 40.54 Wh/kg and a P of

6788 W/kg [38]. Thus, the strategy to construct a composite with a rational design can effectively improve the electrochemical properties of materials [39].

Despite the progress made with cobalt-based sulfides and oxides, developing innovative materials with distinctive structures and enhanced catalysis for electrochemical applications remains crucial. In this study, cobalt oxide (Co_3O_4) and cobalt sulfide (Co_3S_4) were combined to form a Co_3O_4/Co_3S_4 nanocomposite using a simple mechanical alloying method. The Cs values at 0.5 A/g were 97.8 F/g for Co_3O_4, 409.8 F/g for Co_3S_4, and 722.9 F/g for the Co_3O_4/Co_3S_4 composite. The composite Co_3O_4/Co_3S_4 EMs exhibited enhanced electrochemical properties compared to the individual Co_3O_4 and Co_3S_4 electrode materials.

2. Materials and methods

Cobalt chloride ($CoCl_2$) by Sigma Aldrich, sodium hydroxide (NaOH), and sodium sulfide ($Na_2S.xH_2O$) from BDH were used as starting materials. Deionized (DI) water and ethanol were used as solvents and washing agents.

The Co_3O_4 nanoparticles were prepared using the sol-gel method. In this process, cobalt chloride and sodium hydroxide (in a 1:2 molar ratio) were each liquefied in 100 ml of distilled water. The cobalt chloride solution was stirred constantly at 60°C while the sodium hydroxide solution was added slowly. The mixture was then heated at 80°C for half an hour and repeatedly washed to eliminate impurities. The final product was air-dried and then annealed at 500°C for 2 hours to improve crystallinity. The sample was subsequently ground to form powder for further characterization.

The Co_3S_4 nanoparticles were synthesized using the co-precipitation method. Solutions of cobalt chloride and sodium sulfide (in a 1:1 molar ratio) were prepared by dissolving each salt in 100 ml of distilled water, followed by constant stirring for 30 minutes. These solutions were then combined and stirred for an additional hour at 60°C, leading to the formation of light purple precipitates. The precipitates were thoroughly washed multiple times to remove impurities. The final product was dried and calcined at 500°C for 2 hours to enhance its crystallinity. It was then ground into a fine powder for characterization.

A simple mechanical alloying method was employed to synthesize the Co_3O_4/Co_3S_4 nanocomposite. Equal ratios of cobalt oxide and cobalt sulfide were mechanically mixed for 3 hours. The resulting composite was then collected for further analysis.

2.1. Sample characterization

The structural study of materials was carried out by Bruker D8 x-ray diffractometer (XRD) equipped with Cuk_α radiations of 0.154 nm. The morphology of nanostructures was studied by TESCAN Mira3 field emission scanning electron microscope (SEM). Optical properties were studied by Photoluminescence measurements (Melles Griot Series 56). Raman spectrum (Dongwoo) was carried out with by confocal mapping system. The electrochemical measurements were carried out by the Voltalab (PGZ 402) system.

2.2. Electrochemical studies

A three-electrode system has been employed to explore the electrochemical properties of the synthesized nanostructures for cyclic voltammetry (CV), galvanostatic charge-discharge (GCD), and Electrochemical impedance spectroscopy (EIS) measurements. Prepared Co_3O_4, Co_3S_4, and Co_3O_4/Co_3S_4 nanostructures used as working electrodes, Pt used as counter electrodes, and Ag/AgCl used as reference electrodes.

The values of, Cs, Ed, and Pd were measured from GCD using given equations.

$$\text{(Specific capacitance) } Cs = \frac{I.\Delta t}{m.\Delta V} \tag{i}$$

$$\text{(Energy density) } E = \frac{Cs.\Delta V^2}{7.2} \tag{ii}$$

$$\text{(Power density) } P = \frac{3600.E}{\Delta t} \tag{iii}$$

where,

- Cs = specific capacitance
- I = Current
- Δt = discharge time
- ΔV = potential change
- M = Active mass
- E = energy density
- P = power density

3. Results and discussion

The crystalline structure of the prepared cobalt oxide nanostructures was studied utilizing XRD, as represented in Figure 1. The XRD band of the cobalt oxide sample shows the cubic phase of Co_3O_4 nanostructures with a space group of Fd3m. The observed XRD peaks at diffraction angles 2θ = 31.2°, 36.8°, 38.5°, 44.8°, 55.6°, 59.3°, and 65.2° correspond to the (220), (311), (222), (400), (511), and (440) planes, respectively. These peaks confirm the cubic phase of Co_3O_4 nanoparticles, consistent with the standard data card (JCPDS number 43-1003). Similar findings have been reported by other researchers as well [40]'[41].

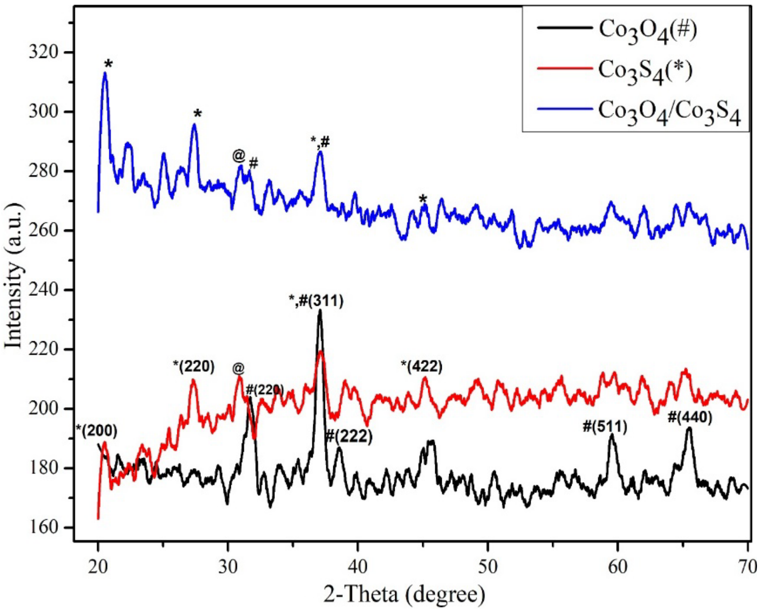

Fig. 1. XRD pattern of prepared Co_3O_4, Co_3S_4 and their composite Co_3O_4/Co_3S_4.

The XRD pattern in Figure 1 depicts the crystalline structure of cobalt sulfide nanoparticles. The pattern indicates a face-centered cubic structure for cobalt sulfide. Detected XRD peaks at diffraction angles 2θ = 20.52°, 27.38°, 37.06°, and 45.12° correspond to the (200), (220), (311), and (331) planes, respectively, confirming the presence of Co_3S_4. These findings align with standard reference cards [JCPDS 75-1561]. Additionally, a single peak at 31.2° signifies the crystalline primitive hexagonal CoS phase, indicated by the @ sign. Comparable results have been observed in previous studies by other researchers [42] who have seen the co-existence of CoS2, CoS, and Co3S4 nanoparticles after preparation making it difficult to obtain pure cobalt sulfide phase Co_mS_n due to complex stoichiometry of various such compounds [43], [44]. In the XRD graph of the Co_3O_4 and Co_3S_4 Nanocomposite, "#" and "*" represent the presence of Co_3O_4 and Co_3S_4, respectively. The peaks at 2θ = 31.2° and 36.8° correspond to the (220) and (311) planes of Co_3O_4, while peaks at 2θ = 20.52°, 27.38°, 37.06°, and 45.12° correspond to the (200), (220), (311), and (331) planes of Co_3S_4, respectively. These peaks confirm the presence of both Co_3O_4 and Co_3S_4 in the nanocomposite, validating its successful synthesis.

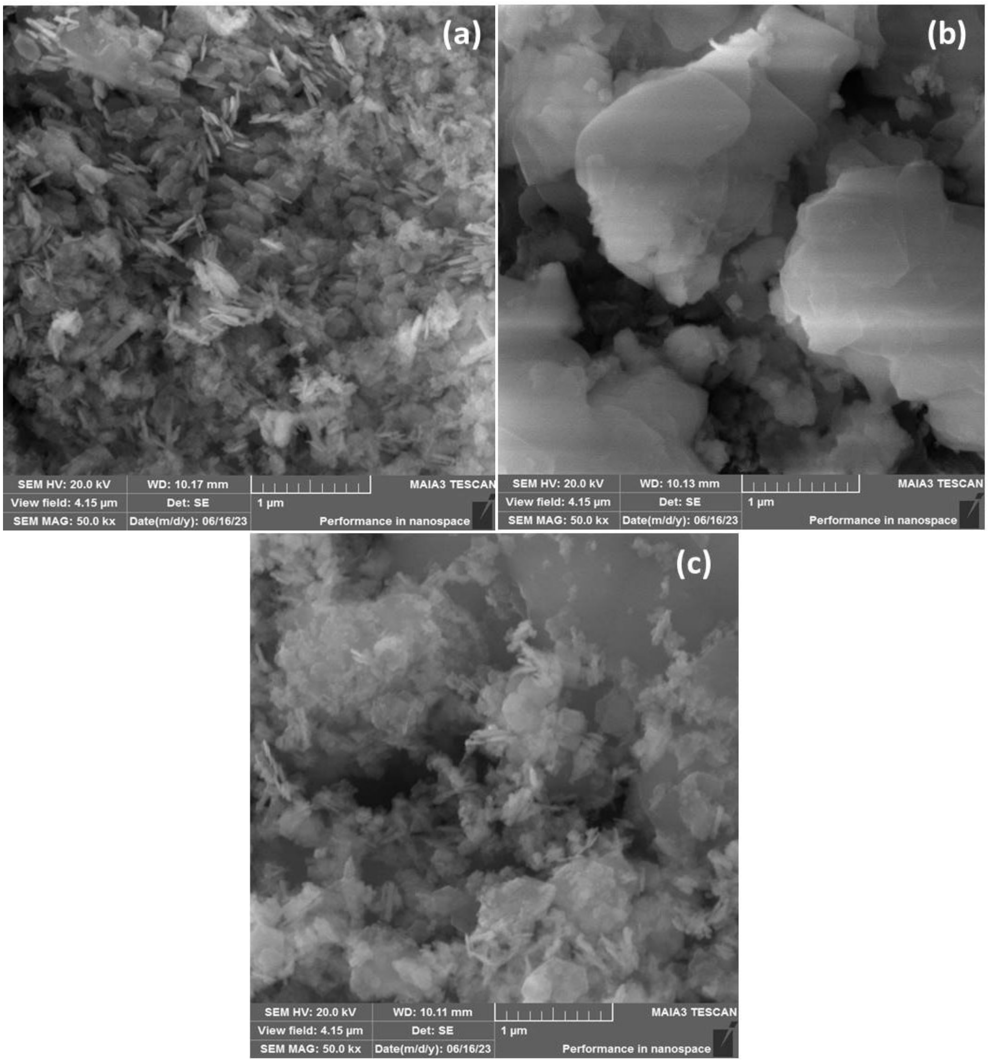

Fig. 2. SEM images of (a) Co_3O_4 (b) Co_3S_4 (c) Co_3O_4/Co_3S_4, at 500 nm.

The figure 2(a,b,c) depicts scanning electron micrographs at a magnification of 1000 nm, showing the surface morphology of Co_3O_4, Co_3S_4, and Co_3O_4/Co_3S_4 nanoparticles. Analysis reveals a nano-rod-like shape for Co_3O_4, a sphere-like morphology for Co_3S_4, and both sphere-like and nano-rod-like shapes are seen in the composite, as observed in Figures 2- (a), (b), and (c), respectively. This indicates the successful synthesis of the Co_3O_4/Co_3S_4 nano-composite.

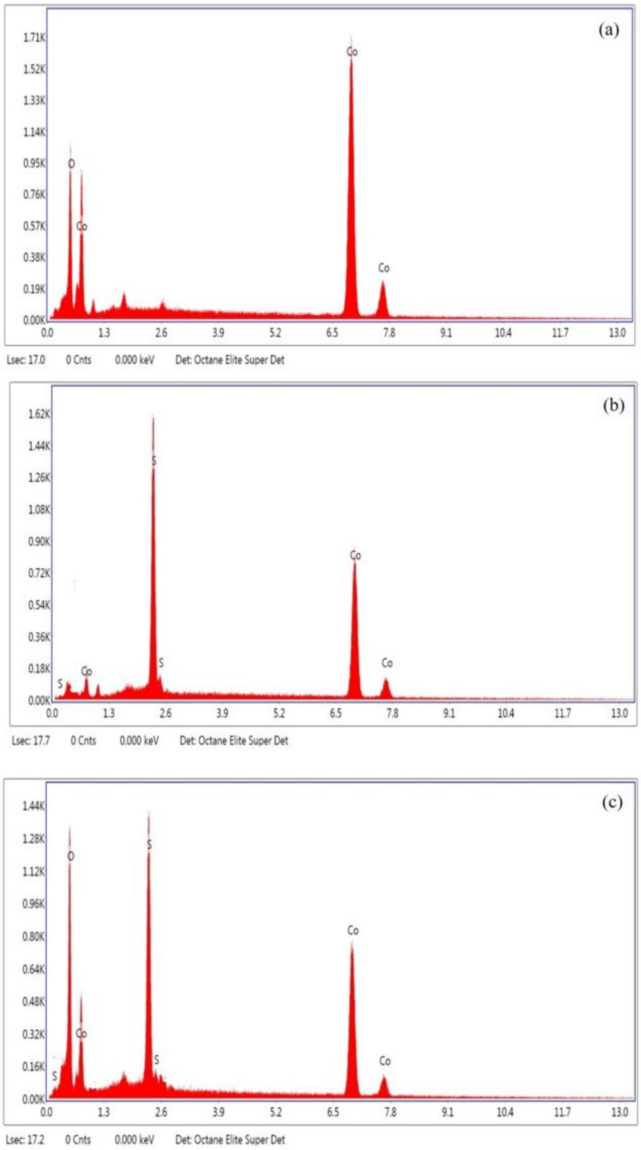

Fig. 3 EDS spectra of (a) Co_3O_4*, (b)* Co_3S_4*, and (c)* Co_3O_4/Co_3S_4*.*

EDX was used to measure the composition of elements in the prepared samples. Figure, 3(a,b,c) shows each element's composition in the synthesized sample. EDX analysis shows that Co_3O_4, Co_3S_4, and Co_3O_4/Co_3S_4 samples consisting of Co, O, and S elements confirm the successful formation of concerned nano-particles.

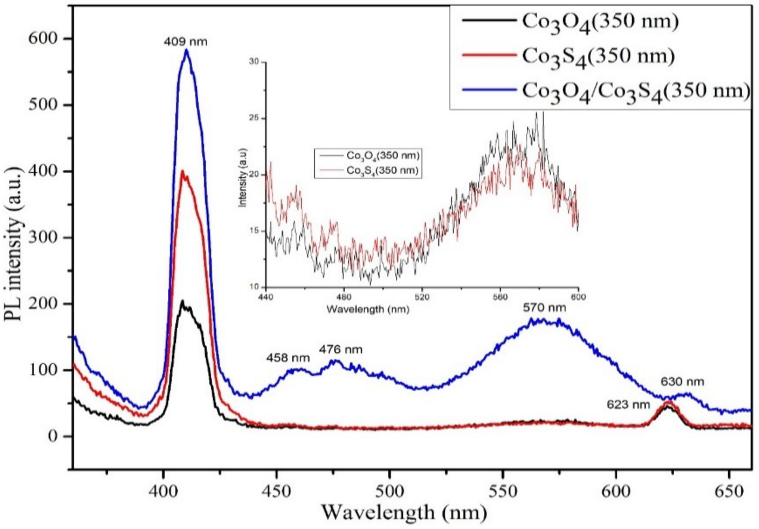

Fig. 4. PL spectra of Co_3O_4, Co_3S_4, and Co_3O_4/Co_3S_4 at 350 nm.

The photoluminescence (PL) spectrum is the best analysis tool to detect defects such as oxygen vacancies and interstitials. The size, formation conditions, and morphology of crystals may change surface states and the density of defects [45]. The high-intensity emission of the nano-composite is because of the fast recombination rate of the charge carriers [46]. It is interesting to observe different defect energy levels. The photoluminescence spectra of the prepared nanostructures (Co_3O_4, Co_3S_4, and their nano-composite) revealed a common high-intensity strong UV emission from the bottom of the conduction band (BCB) to the top of the valence band (TVB) at 409 nm which is due to the exciton recombination through an exciton-exciton collision process [47]. The emission peaks at 458 and 478 nm are due to the transition from the state of Co^{+3} which is from, below the BCB to the TVB [48]. The peak position at 570 nm is attributed to the deep-level green emission from crystal defects. This green emission is mainly due to point defects and free electron concentration [49]. This defect might be associated with the transition from donors' cobalt interstitials, and oxygen vacancy to accepters' cobalt vacancy, and oxygen interstitials [50].

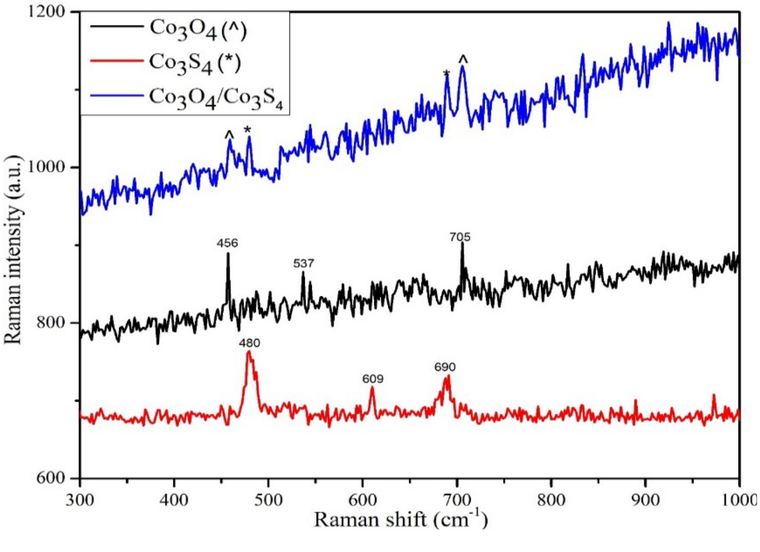

Fig. 5. Raman spectra of Co_3O_4, Co_3S_4, and Co_3O_4/Co_3S_4.

The Raman graph of Co_3O_4 reveals three distinct peaks centered at 456 cm^{-1} (E_g mode), 537 cm^{-1} ($F^{(2)}_{2g}$ mode), and 705 cm^{-1} (A_{1g} mode), which correspond to the distinctive characteristics of the cubic Co_3O_4 phase. The band centered at 705 cm^{-1} (A1g mode) is assigned to the octahedral (CoO_6) site, corresponding to the vibrational mode of O^7_h spectroscopic symmetry. These vibrational Raman bands reveal the same characteristic bands as those reported earlier for the cubic Co_3O_4 structure [51], [52].

The Raman peaks of Co_3S_4 are positioned at 480 cm^{-1}, 609 cm^{-1}, and 690 cm^{-1}, consistent with the E_g, F_{2g}, and A_{1g} modes, respectively. These characteristic peaks are associated with the Co_3S_4 structure in the earlier report [53], [54]. These results align well with the XRD data for Co_3S_4.

The typical peaks of Co_3O_4 centered at 456 cm^{-1} and 705 cm^{-1}, and that of Co_3S_4 centered at 480 cm^{-1} and 690 cm^{-1}, are present in the Co_3O_4/Co_3S_4 nano-composite. These peaks can be well attributed to the vibration modes of each composition.

CV, EIS, and GCD measurements are employed to elucidate the electrochemical properties of the synthesized EMs for practical use in efficient supercapacitors.

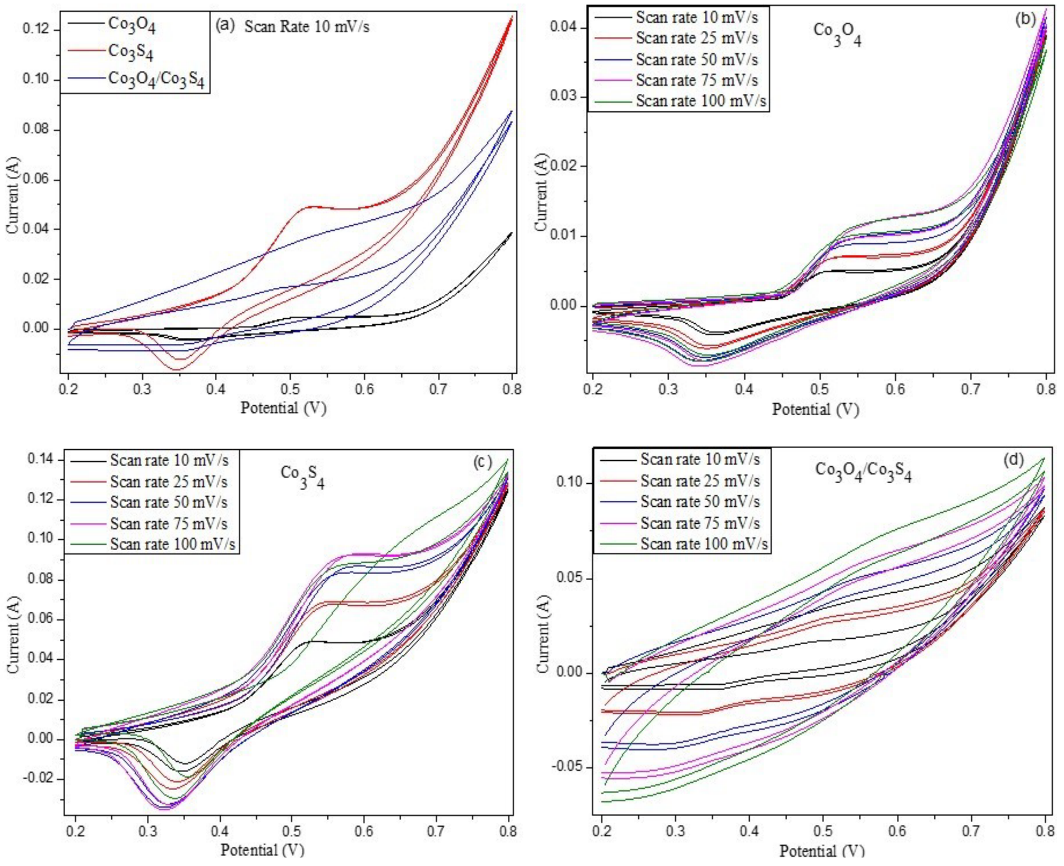

.Fig. 6. (a) CV measurements of synthesized Co_3O_4, Co_3S_4, and Co_3O_4/Co_3S_4 composite at 10 mV/s scan rate. CV measurements of synthesized (b) Co_3O_4, (c) Co_3S_4, and (d) Co_3O_4/Co_3S_4 composite at scan rate ranges from 10-100 mV/s.

We calculated the electrochemical properties of the fabricated Co_3O_4, Co_3S_4, and Co_3O_4/Co_3S_4 composite nanostructures through CV analysis to reveal their supercapacitor properties. The figure 6(a,b,c,d) displays the results of the Co_3O_4, Co_3S_4, and Co_3O_4/Co_3S_4 electrodes analyzed at several scan rates (alternating from 10 to 100 mV/s) in the voltage range from 0.2-0.8 V in an aqueous solution of 2M KOH. During electrochemical reactions, these cobalt-containing materials (Co_3O_4 and Co_3S_4) clearly show the redox behaviors of the metals. This redox behavior was also seen in an earlier report [55]. The faradaic effect comprises ion immigration combined with surface-bound redox capacitance, while the non-faradaic process results from double-layer capacitance [56]. Spanning the scan rate from low to high value can enhance the potential of the redox peak, as evidenced by fast-redox reactions that might be happening at the interface between the electrolyte ions and electrode materials. The consequences of the CV curves for Co_3O_4 and Co_3S_4 composite show reduction and oxidation peaks. The sharpness of these peaks indicates the reaction rate. The cathodic and anodic peaks increased with higher sweep rates, yet their positions remained consistent, suggesting bidirectional ion migration [57]. The redox behavior of Co_3O_4 and Co_3S_4 indicates the pseudocapacitive nature of these electrode materials. Upon careful analysis of the CV results for the Co_3O_4/Co_3S_4 EMs, it was observed that the composite electrodes exhibited a combined contribution of double-layer and pseudocapacitive behavior, showing ideal capacitive properties with broader redox peaks and a quasi-rectangular shape. The interaction between Co_3O_4 and Co_3S_4 phases in the composite may create a structure that enables both double-layer and pseudocapacitive charge storage, which may contribute to reduced internal resistance and more stable performance, beneficial for practical energy storage applications.

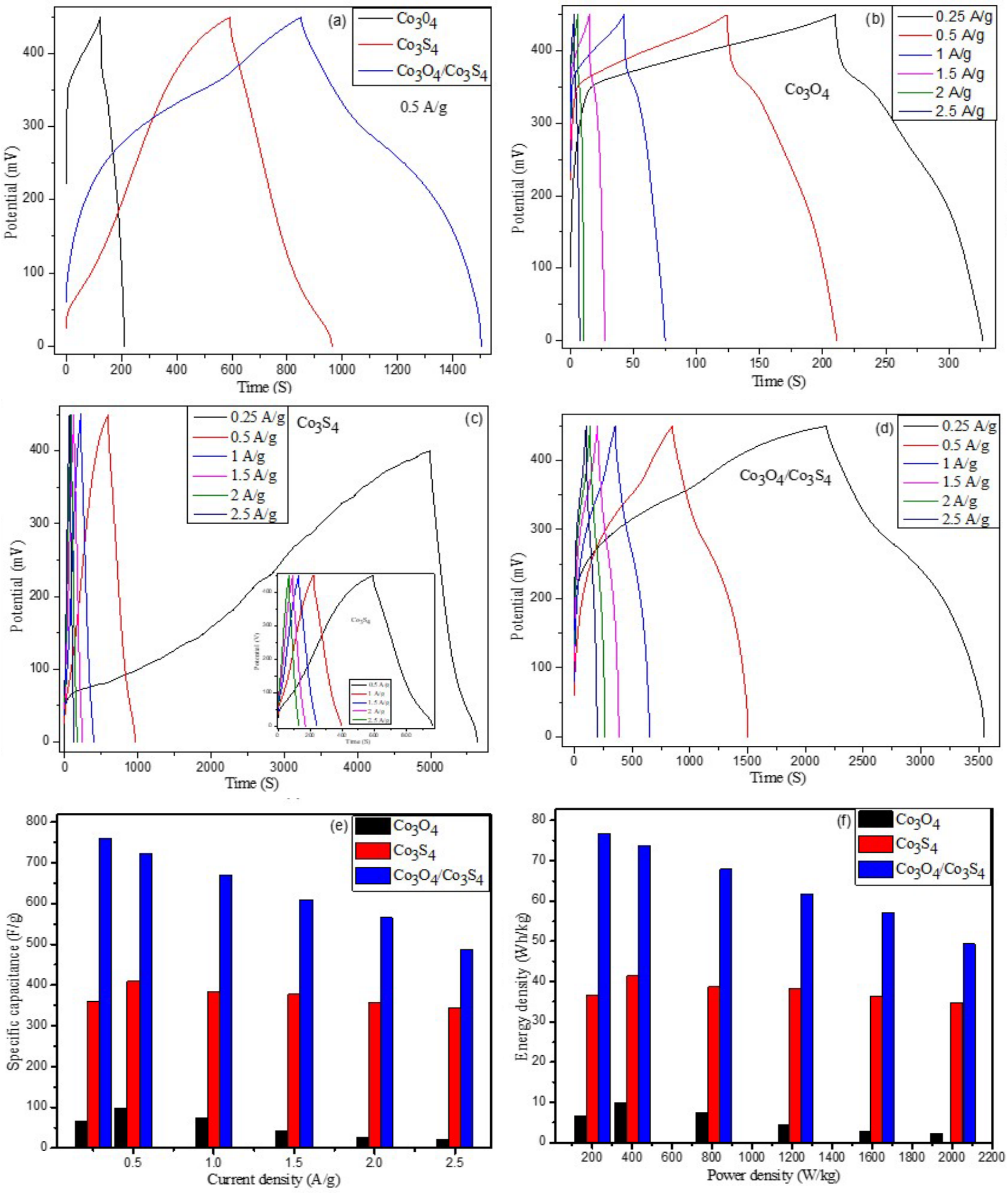

Fig. 7. GCD curves of synthesized Co_3O_4, Co_3S_4, and Co_3O_4/Co_3S_4 composite at 0.5 A/g. GCD curves of synthesized (b) Co_3O_4, (c) Co_3S_4, and (d) Co_3O_4/Co_3S_4 composite from 0.25-2.5 A/g. (f) specific capacitance of synthesized Co_3O_4, Co_3S_4, and Co_3O_4/Co_3S_4 composite 0.25-2.5 A/g. (g) Energy-power densities of synthesized Co_3O_4, Co_3S_4, and Co_3O_4/Co_3S_4 composite.

The galvanostatic charge-discharge (GCD) experiment was performed (from 0.25 to 2.5 A/g) to measure the electrochemical supercapacitor properties of the electrode materials. Figure 7(a, b, c, d) represents the charge-discharge profiles of the Co_3O_4, Co_3S_4, and Co_3O_4/Co_3S_4 EMs at different current densities. The presence of two potential plateaus for Co_3O_4 and Co_3S_4 confirms the faradaic redox reactions, while the approximately linear and triangular shape of Co_3O_4/Co_3S_4 indicates capacitive behavior, supporting the CV results. All the GCD graphs exhibit symmetrical behavior, suggesting reversible charge-discharge properties.

The determined Cs values (F/g) are shown in Figure 7(e). The Cs values at 0.5 A/g are 97.8 F/g for Co_3O_4, 409.8 F/g for Co_3S_4, and 722.9 F/g for the Co_3O_4/Co_3S_4 composite. The capacitance value of the composite EMs is significantly higher than that of Co_3O_4 and Co_3S_4, likely due to the more electroactive surfaces between the electrode and electrolyte. These sites facilitate the transport of electrons and ions during the charging and discharging process. Energy densities of 9.9, 41.5, and 73.8 Wh/kg were achieved at power densities of 405, 405.1, and 405 W/kg for the Co_3O_4, Co_3S_4, and Co_3O_4/Co_3S_4 electrode materials, respectively.

Table 1. Synthesized electrode materials comparison with reported literature for SCs systems.

Material	Specific capacitance (F/g)	Current density (A/g)	Energy Density (Wh/kg)	Power density (W/kg)	Capacitance retention (%)	No. of Cycles	Reference
Co_3O_4	97.8	0.5	9.9	405	98.5	1500	This work
Co_3S_4	409.8	0.5	41.5	405.1	74	1500	This work
Co_3O_4/ Co_3S_4	722.9	0.5	73.8	405	98	1500	This work
Co_3O_4	98.39	0.66	18	200	94	5000	[58]
Co_3O_4 (SCS-R)	278	1	111.58	869.45	90	6000	[59]
Co_3O_4@NPCS	464	1	98.5	1500	87.2	10000	[60]
Co_3O_4/AC	125	1	25.27	585	93.75	8000	[61]
Co_3S_4 polyhedra	668	1	20.7	716	81.4	2000	[62]
Co_3S_4/WS_2 composite	412.7	1	47.3	512	92	2000	[63]
Co_3S_4/Ni_3S_4	617.78	0.5	40.54	6788			[38]
MnS/Co_3S_4	627	1			93.2	2000	[64]
(MXene)/$CoS_2/CuCo_2$ S4	706.5	1	42.2	800	96	10000	[65]
Mn-doped Co_3O_4	537	1.5			94	1500	[66]

The composite material maintained an E of 73.8 Wh/kg even at a P of 405 W/kg. Among Co_3O_4, Co_3S_4, and their composite (Co_3O_4/Co_3S_4), the composite electrode exhibited higher Cs and maintained E at high P, demonstrating the best electrochemical supercapacitive performance.

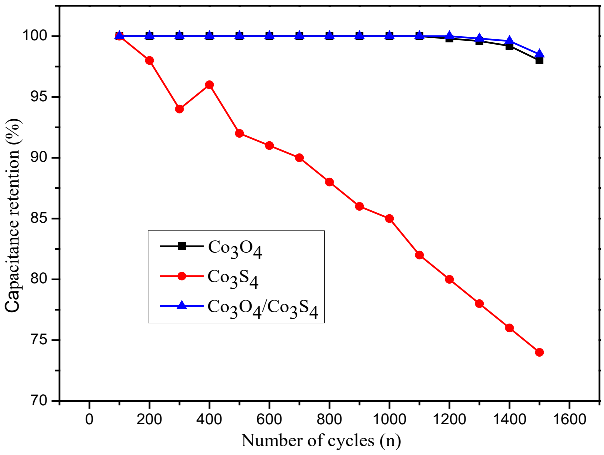

Fig. 8. Capacitance retention of synthesized Co_3O_4, Co_3S_4, and Co_3O_4/Co_3S_4 composite over 1500 charge-discharge cycles at 50 A/g.

The electrochemical stability of Co_3O_4, Co_3S_4, and Co_3O_4/Co_3S_4 composite electrode materials was tested over 1500 Charge-discharge cycles at a high current density of 50 A/g as shown in Figure 7(g). The capacitance value of Co_3S_4 drastically decreased to 74% of initial capacitance after 1500 cycles, whereas Co_3O_4 and Co_3O_4/Co_3S_4 retained about 98.5% and 98% of initial capacitance, respectively, which was higher than that of Co_3S_4. Thus, the composite Co_3O_4/Co_3S_4 exhibits high stability, making it an excellent candidate for electrochemical supercapacitor applications.

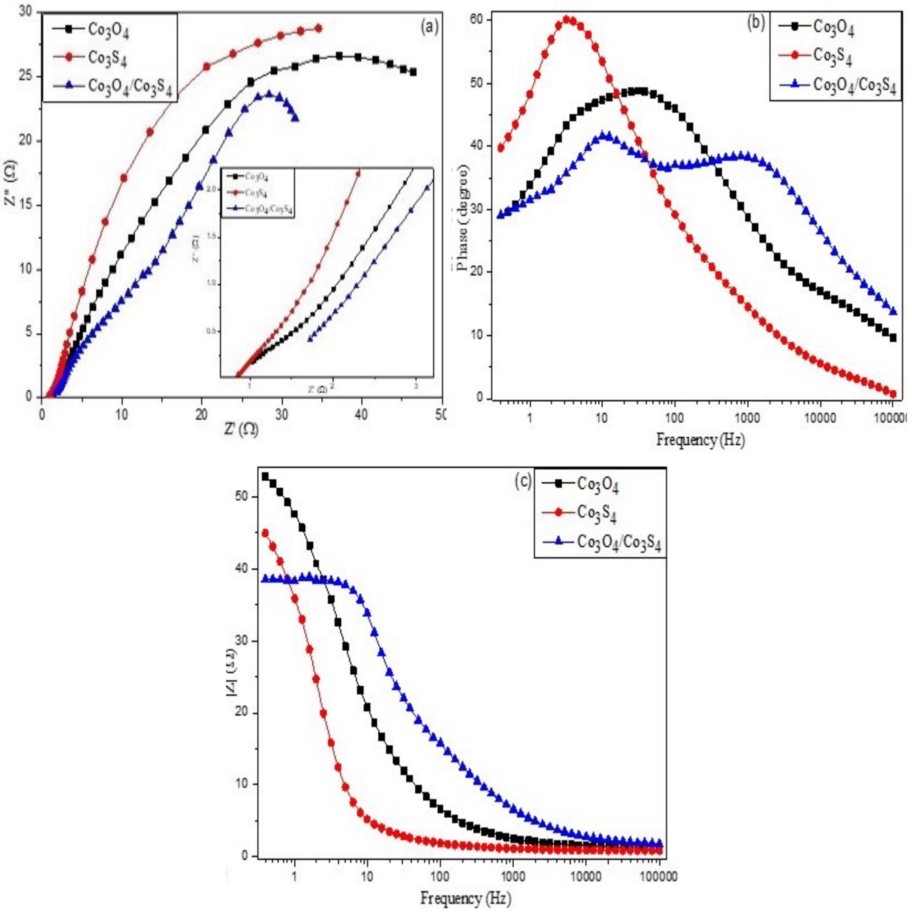

Fig. 9. (a) Nyquist plot of synthesized Co_3O_4, Co_3S_4, and Co_3O_4/Co_3S_4 composite. (b) bode-modulus impedance plot of synthesized Co_3O_4, Co_3S_4, and Co_3O_4/Co_3S_4 composite. (c) bode-phase plot of synthesized Co_3O_4, Co_3S_4, and Co_3O_4/Co_3S_4 composite.

Figure 8(a,b,c) represents the EIS curves of the electrodes. A Nyquist plot typically comprises three fundamental components, each corresponding to different resistances encountered in EIS testing. The x-intercept on the real axis (Z′) of the Nyquist plot signifies the equivalent series resistance (ESR), which includes the inherent resistance of the electrode and the contact resistance between the electrolyte and the sample. The semicircular portion represents the charge transfer resistance (Rct), indicating the resistance encountered by charges as they move between different phases. Furthermore, the location and angle of the diagonal line reveal the mass transport resistance (Warburg resistance, Rw) and highlight the electrode's capacitive behavior, whether, it is ideal or non-ideal [67].

To assess the internal resistance and capacitance of the prepared Co_3O_4, Co_3S_4, and Co_3O_4/Co_3S_4 electrodes, EIS was accompanied across a frequency range spanning from 0.1Hz to 100 kHz. In the Nyquist plot, the solution resistance (Rs) is determined from the x-axis intercept at high frequencies, the Rct is inferred from the semicircle's diameter, and ion diffusion is assessed based on the slope of the linear region at low frequencies. Insight from the Nyquist plot analysis of the sample electrode reveals a slight deviation towards the x-intercept, with estimated Rs values of 1.6 Ω for Co_3O_4 and 1.4 Ω for Co_3S_4. In contrast, the Co_3O_4/Co_3S_4 composite displays a nearly vertical line, suggesting an almost negligible Rct. The Co_3O_4/Co_3S_4 composite displays a nearly vertical line indicative of capacitive behavior and ion diffusion process, which transitions to Rw in the mid-frequency range before deviating toward the impedance axis. This response may result from phase variations within the composite, as confirmed by the XRD analysis. The higher Warburg angle is attributed to the diffusion process occurring at the electrode-electrolyte interfaces, indicating the capacitive behavior of the electrodes.

The Bode plots provide insights into impedance, frequency, and phase angle, with the frequency (f) axis being logarithmic. Significantly, the impedance observed at low frequencies is strongly associated with the polarization resistance (Rct), which is influenced by the kinetics of the electrode reactions [68]. The frequency-phase plot provides valuable insights into the electrochemical behavior of the material: at high frequencies, it reveals capacitive or resistive characteristics; in the mid-frequency region, it reflects charge transfer efficiency; and at low frequencies, it indicates diffusion-controlled processes. The composite exhibits a higher phase angle in the high-frequency region in the Bode frequency-phase plot, indicating its capacitive behavior. In the mid-frequency region, the composite exhibits two distinct peaks. These peaks indicate separate charge transfer and ion diffusion processes, suggesting contributions from both faradaic and capacitive mechanisms, as corroborated by the CV analysis. These distinct peaks may be attributed to additional phase layers, as identified in the XRD analysis. This behavior has also been reported in previous studies, where it was observed to result from interfacial states formed at the interfaces [69]. The composite material exhibits multiple phase layers, providing multiple charge storage pathways that are beneficial for energy storage applications in supercapacitors.

In Figure 8(c), the composite exhibits a lower modulus impedance compared to the individual Co_3O_4 and Co_3S_4 materials, suggesting that the composite has lower charge transfer resistance and enhanced ion diffusion. At a certain frequency, the composite shows a constant behavior, which could indicate stable capacitance or pseudocapacitive behavior. This may be due to improved interfacial charge transfer at the boundaries between Co_3O_4 and Co_3S_4, with the presence of multiple phases also confirmed by XRD and SEM images of the composite. The Co_3O_4 and Co_3S_4 composite may have formed a structure with optimized ion transport pathways and stable charge storage zones at their interfaces, implying reduced energy loss and stable electrochemical performance, which could make it suitable for practical energy applications.

4. Conclusions

In this study, Co_3O_4, Co_3S_4, and a Co_3O_4/Co_3S_4 composite were synthesized using sol-gel, co-precipitation, and mechanical alloying methods, respectively, and their electrochemical properties as potential electrode materials were evaluated. XRD and Raman analyses confirmed the cubic phase of Co_3O_4 and the face-centered cubic phase of Co_3S_4, with a multiphase structure in the Co_3O_4/Co_3S_4 composite due to the presence of both phases. SEM images revealed rod-like and spherical morphologies for Co_3O_4 and Co_3S_4, respectively, while the composite exhibited both forms, suggesting a multiphase structure. EDX confirmed the elemental composition, while photoluminescence (PL) analysis identified multiple defects such as oxygen vacancies, interstitials, and phase boundaries in the composite, likely due to the stoichiometric and kinetic distinctions between Co_3O_4 and Co_3S_4.

The electrochemical analysis highlighted the Co_3O_4/Co_3S_4 composite's superior performance. Cyclic voltammetry (CV) revealed redox peaks in Co_3O_4 and Co_3S_4, indicating pseudocapacitive behavior, while the Co_3O_4/Co_3S_4 composite displayed a quasi-rectangular shape with small peaks, suggesting a combined contribution from pseudocapacitance and electric double-layer capacitance. GCD measurements showed Cs of 97.8 F/g for Co_3O_4, 409.8 F/g for Co_3S_4, and 722.9 F/g for the Co_3O_4/Co_3S_4 composite at 0.5 A/g. The composite also achieved an Ed of 73.8 Wh/kg at a Pd of 405 W/kg, significantly surpassing Co_3O_4 and Co_3S_4 at similar power densities. Furthermore, EIS showed that the composite exhibited negligible charge transfer resistance (Rct), compared to 1.6 Ω for Co_3O_4 and 1.4 Ω for Co_3S_4, highlighting enhanced charge transfer capabilities.

Bode-phase plot analysis for the composite showed two distinct phases in the mid-frequency range, suggesting multiple reaction kinetics, likely linked to ion diffusion and charge transfer processes. Bode-modulus impedance measurements revealed lower and stable impedance for the composite over a specific frequency range, indicating stable charge storage behavior and enhanced electrochemical stability. The composite also demonstrated excellent cycling stability, retaining 98.5% of its capacitance after 1500 cycles at 50 A/g, outperforming Co_3O_4 (98%) and Co_3S_4 (78%).

Overall, the Co_3O_4/Co_3S_4 composite's high specific capacitance, superior energy density, stable high-power performance, low Rct, and robust cycling stability underline its potential as an efficient and durable energy storage material. These findings underscore the synergistic benefits arising from the combined Co_3O_4 and Co_3S_4 phases, positioning the composite as the best option for practical energy storage devices.

Funding

Researchers supporting the project (RSP2025R118) at King Saud University.

Acknowledgments

The authors extend their appreciation to the Researchers Supporting Project number (RSP2025R118) of King Saud University, Riyadh, Saudi Arabia.

References

[1] I. Melkiyur et al., Renew. Sustain. Energy Rev., 173, 113106 (2023); https://doi.org/10.1016/j.rser.2022.113106

[2] Y.-C. Lu et al., Energy Environ. Sci., 6(3), 750(2013); https://doi.org/10.1039/c3ee23966g

[3] K. Chayambuka, G. Mulder, D. L. Danilov, P. H. L. Notten, Adv. Energy Mater 10(38), 2001310 (2020); https://doi.org/10.1002/aenm.202001310

[4] J. Chen, P. S. Lee, Adv. Energy Mater 11(6), 2003311 (2021).

[5] J. Zhao, A. F. Burke, J. Energy Chem., 59, 276 (2021); https://doi.org/10.1016/j.jechem.2020.11.013

[6] S. Ahankari, D. Lasrado, R. Subramaniam, Mater. Adv 3(3), 1472 (2022); https://doi.org/10.1039/D1MA00599E

[7] P. Poizot, J. Gaubicher, S. Renault, L. Dubois, Y. Liang, Y. Yao, Chem. Rev 120(14), 6490 (2020); https://doi.org/10.1021/acs.chemrev.9b00482

[8] H. Cheng et al., Prog. Polym. Sci 106, 101253 (2020); https://doi.org/10.1016/j.progpolymsci.2020.101253

[9] R. Liang et al., Nanomaterials 11(5), 1248 (2021); https://doi.org/10.3390/nano11051248

[10] Y. Gao, L. Zhao, Chem. Eng. J 430, 132745 (2022); https://doi.org/10.1016/j.cej.2021.132745

[11] B. K. Saikia, S. M. Benoy, M. Bora, J. Tamuly, M. Pandey, D. Bhattacharya, Fuel 282, 118796 (2020); https://doi.org/10.1016/j.fuel.2020.118796

[12] Z. Ling et al., Nanoscale 7(12), 5120 (2015); https://doi.org/10.1039/C5NR00081E

[13] C. Xia, W. Chen, X. Wang, M. N. Hedhili, N. Wei, H. N. Alshareef, Adv. Energy Mater 5(8), 1401805 (2015); https://doi.org/10.1002/aenm.201401805

[14] S. Yuan et al., Energy Storage Mater 42, 317 (2021); https://doi.org/10.1016/j.ensm.2021.07.007

[15] J. Ma et al., Adv. Funct. Mater 32(4), 2107439 (2022).

[16] U. Anwar, N.A. Noor, S. Mumtaz, I.M. Moussa, Chalcogenide Lett., vol. 22, no. 3, pp. 261-276, 2025; https://doi.org/10.15251/CL.2025.223.261

[17] S. Thampy, N. Ashburn, K. Cho, J. W. P. Hsu, Adv. Energy Sustain. Res 2(4), 2000075 (2021); https://doi.org/10.1002/aesr.202170011

[18] M. Tawalbeh, H. A. Khan, A. Al-Othman, J. Energy Storage 60, 106656 (2023). https://doi.org/10.1016/j.est.2023.106656

[19] X. Wang et al., Crystals 10(9), 720 (2020); https://doi.org/10.3390/cryst10090720

[20] P. Geng et al., Adv. Energy Mater 8(15), 1703259 (2018).

[21] Z. Ali, M. Z. Iqbal, H. H. Hegazy, Energy Storage 73, 108857 (2023); https://doi.org/10.1016/j.est.2023.108857

[22] L. Li, S. Jia, M. Cao, Y. Ji, H. Qiu, D. Zhang, Energy Storage 67, 107614 (2023); https://doi.org/10.1016/j.est.2023.107614

[23] R. Mohili, N. R. Hemanth, H. Jin, K. Lee, N. Chaudhari, Mater. Chem. A. 11(20), 10463 (2023); https://doi.org/10.1039/D2TA10081A

[24] T. Wang, H. C. Chen, F. Yu, X. S. Zhao, H. Wang, Energy Storage Mater 16, 545 (2019); https://doi.org/10.1016/j.ensm.2018.09.007

[25] S. Wang et al., Mater. Chem. Front., (2023).

[26] N. Mahmood, C. Zhang, J. Jiang, F. Liu, Y. Hou, Chem. - Eur. 19(16), 5183 (2013); https://doi.org/10.1002/chem.201204549

[27] R. Barik, P. P. Ingole, Curr. Opin. Electrochem. 21, 327 (2020); https://doi.org/10.1016/j.coelec.2020.03.022

[28] X. Y. Yu, X. W. (David) Lou, Adv. Energy Mater. 8(3), 1701592 (2018).

[29] H. Osgood, S. V. Devaguptapu, H. Xu, J. Cho, G. Wu, Nano Today 11(5), 601 (2016); https://doi.org/10.1016/j.nantod.2016.09.001

[30] X. Wang et al., ChemElectroChem 5(2), 309-315(2018); https://doi.org/10.1002/celc.201701050

[31] W. K. Chee, H. N. Lim, Z. Zainal, N. M. Huang, I. Harrison, Y. Andou, Phys. Chem. C 120(8), 4153 (2016); https://doi.org/10.1021/acs.jpcc.5b10187

[32] Z. Yan et al., Electrochimica Acta 251, 235 (2017); https://doi.org/10.1016/j.electacta.2017.03.059

[33] X. Zhao et al., Nanoscale 8(41), 17902 (2016); https://doi.org/10.1039/C6NR05584B

[34] S. Kalpana, V. S. Bhat, G. Hegde, T. Niranjana Prabhu, P. N. Anantharamaiah, Inorg. Chem. Commun. 154, 110984 (2023); https://doi.org/10.1016/j.inoche.2023.110984

[35] M. Zhu, Y. Yang, X. Zhang, Y. Liang, J. Tang, Appl. Organomet. Chem. 38(8), 7533 (2024); https://doi.org/10.1002/aoc.7533

[36] W. Zhang et al., Energy Storage 57, 106170 (2023); https://doi.org/10.1016/j.est.2022.106170

[37] Y. Gu et al., Social Science Research Network, 4698368 (2024).

[38] G. Liu et al., J. Energy Storage 94, 112462 (2024); https://doi.org/10.1016/j.est.2024.112526

[39] J. Yan et al., Electrochimica Acta 55(23), 6973 (2010); https://doi.org/10.1016/j.electacta.2010.06.081

[40] R. Packiaraj, P. Devendran, K. S. Venkatesh, S. Asath Bahadur, A. Manikandan, N. Nallamuthu, J. Supercond. Nov. Magn. 32, 2427 (2019); https://doi.org/10.1007/s10948-018-4963-6

[41] C. I. Priyadharsini et al., J. Sol-Gel Sci. Technol. 96, 416 (2020); https://doi.org/10.1007/s10971-020-05393-x

[42] J. H. Joshi, D. K. Kanchan, M. J. Joshi, H. O. Jethva, K. D. Parikh, Mater. Res. Bull. 93, 63

(2017); https://doi.org/10.1016/j.materresbull.2017.04.013

[43] J. H. Joshi, D. K. Kanchan, M. J. Joshi, H. O. Jethva, K. D. Parikh, Mater. Res. Bull. 93, 63 (2017); https://doi.org/10.1016/j.materresbull.2017.04.013

[44] S. Vijaya, G. Landi, J. J. Wu, S. Anandan, J. Power Sources 478, 229068 (2020); https://doi.org/10.1016/j.jpowsour.2020.229068

[45] C. Ragupathi, L. J. Kennedy, J. J. Vijaya, Adv. Powder Technol. 25(1), 267 (2014); https://doi.org/10.1016/j.apt.2013.04.013

[46] N. R. Khalid et al., Ceram. Int. 48(21), 32009 (2022); https://doi.org/10.1016/j.ceramint.2022.07.138

[47] H. Zhu et al., Environ. Sci. Technol. 54(14), 8601 (2020); https://doi.org/10.1021/acs.est.0c03427

[48] D. Letsholathebe et al., Mater. Today Proc. 36, 499 (2021); https://doi.org/10.1016/j.matpr.2020.05.205

[49] M. Manickam, V. Ponnuswamy, C. Sankar, R. Mariappan, R. Suresh, Silicon 8(3), 351 (2016); https://doi.org/10.1007/s12633-015-9316-5

[50] M. N. Siddique, N. Ahmad, P. Tripathi, Opt. Mater. 107, 110101 (2020); https://doi.org/10.1016/j.optmat.2020.110101

[51] A. G. Abd-Elrahim, D.-M. Chun, Ceram. Int. 46(15), 23479 (2020); https://doi.org/10.1016/j.ceramint.2020.06.118

[52] A. G. Abd-Elrahim, D.-M. Chun, J. Alloys Compd. 853, 156946 (2021); https://doi.org/10.1016/j.jallcom.2020.156946

[53] S. J. Patil, J. H. Kim, D. W. Lee, J. Power Sources 42, 652 (2017); https://doi.org/10.1016/j.jpowsour.2016.12.096

[54] F. Luo, D. Ma, Y. Li, H. Mi, P. Zhang, S. Luo, Electrochimica Acta, 299, 173 (2019); https://doi.org/10.1016/j.electacta.2018.12.175

[55] S. Ramesh, K. Karuppasamy, H.-S. Kim, H. S. Kim, J.-H. Kim, Sci. Rep. 8(1), 16543 (2018); https://doi.org/10.1038/s41598-018-34905-7

[56] S. Dsoke, K. Pfeifer, Z. Zhao, in Frontiers of Nanoscience 19, 99 (2021); https://doi.org/10.1016/B978-0-12-821434-3.00001-6

[57] K. Daub, X. Zhang, L. Wang, Z. Qin, J. J. Noël, J. C. Wren, Electrochimica Acta 56(19), 6661 (2011); https://doi.org/10.1016/j.electacta.2011.05.047

[58] S. Majumder, S. S. Karade, K. H. Kim, Surf. Interfaces 46, 104128 (2024); https://doi.org/10.1016/j.surfin.2024.104128

[59] H. Wang et al., J. Energy Storage 58, 106322 (2023); https://doi.org/10.1016/j.est.2022.106322

[60] A. Arjunan, S. Ramasamy, J. Kim, S.-K. Kim, J. Energy Storage 68, 107758 (2023); https://doi.org/10.1016/j.est.2023.107758

[61] B. A. Al Jahdaly, A. Abu-Rayyan, M. M. Taher, K. Shoueir, ACS Omega 7(27), 23673 (2022); https://doi.org/10.1021/acsomega.2c02305

[62] M. Zhu, Y. Yang, X. Zhang, Y. Liang, J. Tang, Appl. Organomet. Chem. 38(8), 7533 (2024); https://doi.org/10.1002/aoc.7533

[63] V. Shrivastav, S. Sundriyal, P. Goel, V. Shrivastav, U. K. Tiwari, A. Deep, Electrochimica Acta 345, 136194 (2020); https://doi.org/10.1016/j.electacta.2020.136194

[64] L. Fuzhi et al., Electrochimica Acta. 390, 138893 (2021); https://doi.org/10.1016/j.electacta.2021.138893

[65] S. De, C. K. Maity, S. Acharya, S. Sahoo, J.-J. Shim, G. C. Nayak, J. Energy Storage 50, 104617 (2022); https://doi.org/10.1016/j.est.2022.104617

[66] A. Karthikeyan, R. Mariappan, J. Alloys Compd. 968, 172094 (2023); https://doi.org/10.1016/j.jallcom.2023.172094

[67] H. S. Magar, R. Y. Hassan, A. Mulchandani, Sensors 21(19), 6578 (2021);

https://doi.org/10.3390/s21196578
[68] Y. Fang et al., J. Power Sources 300, 285 (2015);
https://doi.org/10.1016/j.jpowsour.2015.09.049
[69] R. P. Toledo, C. E. Dias, D. R. Huanca, W. J. Salcedo, Symposium on Microelectronics Technology and Devices (SBMicro), IEEE, 1 (2017);
https://doi.org/10.1109/SBMicro.2017.8113011